

Supplemental material: Evaluation of MOPITT version 7 joint TIR-NIR X_{CO} retrievals with TCCON

Jacob K. Hedelius¹, Tai-Long He¹, Dylan B. A. Jones¹, Rebecca R. Buchholz², Martine De Mazière³, Nicholas M. Deutscher⁴, Manvendra K. Dubey⁵, Dietrich G. Feist^{6,7}, David W. T. Griffith⁴, Frank Hase⁸, Laura T. Iraci⁹, Pascal Jeseck¹⁰, Matthäus Kiel¹¹, Rigel Kivi¹², Cheng Liu¹³, Isamu Morino¹⁴, Justus Notholt¹⁵, Young-Suk Oh¹⁶, Hirofumi Ohyama¹⁴, David F. Pollard¹⁷, Markus Rettinger¹⁸, Sébastien Roche¹, Coleen M. Roehl¹¹, Matthias Schneider⁸, Kei Shiomi¹⁹, Kimberly Strong¹, Ralf Sussmann¹⁸, Colm Sweeney^{20,21}, Yao Té¹⁰, Osamu Uchino¹⁴, Voltaire A. Velazco^{4,22}, Wei Wang²³, Thorsten Warneke¹⁵, Paul O. Wennberg^{11,24}, Helen M. Worden², and Debra Wunch¹

¹Department of Physics, University of Toronto, Toronto, Canada

²Atmospheric Chemistry Observations & Modeling, National Center for Atmospheric Research, Boulder, Colorado, USA

³Royal Belgian Institute for Space Aeronomy (BIRA-IASB), Brussels, 1180, Belgium

⁴Centre for Atmospheric Chemistry, School of Earth, Atmospheric and Life Sciences, University of Wollongong, Northfields Ave. Wollongong NSW 2522 Australia

⁵Los Alamos National Laboratory, Earth and Environmental Sciences, Los Alamos, NM, USA

⁶Deutsches Zentrum für Luft- und Raumfahrt, Institut für Physik der Atmosphäre, Oberpfaffenhofen, Germany

⁷Max Planck Institute for Biogeochemistry, Jena, Germany

⁸Institute of Meteorology and Climate Research (IMK-ASF), Karlsruhe Institute of Technology, Karlsruhe, Germany

⁹NASA Ames Research Center, Mountain View, CA, USA

¹⁰LERMA-IPSL, Sorbonne Université, CNRS, Observatoire de Paris, PSL Université, 75005, Paris, France

¹¹Division of Geological and Planetary Sciences, California Institute of Technology, Pasadena, CA, USA

¹²Finnish Meteorological Institute, Sodankylä, Finland

¹³University of Science and Technology of China, Hefei, 230026, China

¹⁴National Institute for Environmental Studies (NIES), Tsukuba, Japan

¹⁵University of Bremen, Bremen, Germany

¹⁶National Institute of Meteorological Sciences 33, Seohobuk-ro, Seogwipo-si, Jeju-do 63568, Republic of Korea

¹⁷National Institute of Water and Atmospheric Research, Lauder, New Zealand

¹⁸Karlsruhe Institute of Technology (KIT), Institute of Meteorology and Climate Research (IMK-IFU), Garmisch-Partenkirchen, Germany

¹⁹Japan Aerospace Exploration Agency, Tsukuba, Japan

²⁰Cooperative Institutes for Research in Environmental Sciences, University of Colorado, Boulder, CO, USA

²¹NOAA Earth System Research Laboratory, Boulder, CO, USA

²²Oscar M. Lopez Center for Climate Change Adaptation and Disaster Risk Management Foundation, Inc., Philippines.

²³Key Laboratory of Environmental Optics and Technology, Anhui Institute of Optics and Fine Mechanics, Chinese Academy of Sciences, Hefei, China

²⁴Division of Engineering and Applied Science, California Institute of Technology, Pasadena, California, USA

Correspondence: Jacob K. Hedelius (jacob.hedelius@atmosph.physics.utoronto.ca)

S1 Stratospheric contribution to MOPITT priors

From 50–0 hPa there is insufficient information in MOPITT data to retrieve a layer value. Instead this layer is taken from the a priori when creating the column product. The mass ratio of CO in this layer compared to the total column of CO for 2017 is shown in Fig. S1a. We also use the blended tropopause height from the The Modern-Era Retrospective analysis for
5 Research and Applications, Version 2 (MERRA-2) to calculate the stratospheric fraction to the total (Fig. S1b). In general the contribution in the NH is lower than in the SH, and the contribution in the tropics where the tropopause is higher is lower than the rest of the world.

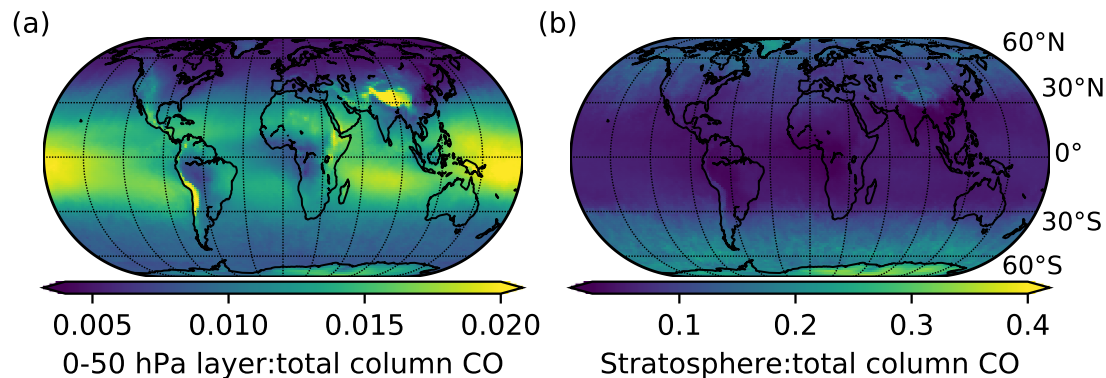


Figure S1. Mass fractions of CO from the stratosphere compared to the total column in the MOPITT priors for 2017. (a) The fraction of the uppermost layer to the total. (b) Fraction of the stratosphere as defined by the MERRA-2 blended tropopause height to the total.

S2 TCCON CO scaling to WMO

Tying column measurements from TCCON to the WMO scale from aircraft measurements is a challenge due to the heterogeneity of atmospheric CO, and lack of stability of CO in cylinders. The heterogeneity of CO means assumptions with large uncertainty may need to be made about CO volume mixing ratios to fill gaps in atmospheric profiles. Usually these gaps are near the surface or in the upper atmosphere beyond the aircraft ceiling. In cylinders CO may change with time. The WMO scale has been periodically updated to tie to gravimetric standards and to account for drift. In the early 1990s measurements were tied to the WMO 88 scale, also known as the CMDL (Climate Monitoring and Diagnostics Laboratory) scale (Novelli et al., 2003). This scale has been updated several times (e.g, WMO-2000, WMO-CO-X2004 (GAW, 2010), WMO-CO-X2014, WMO-CO-X2014A (Zellweger et al., 2017)), which has made small but important improvements. There are also other independent scales that in situ or flask measurements may be tied to such as the Commonwealth Science and Industrial Research Organization (CSIRO) carbon monoxide calibration scale. The next WMO-CO scale update is expected in late 2019 (https://www.esrl.noaa.gov/gmd/ccl/co_scale_update.html, last accessed: 10 December 2018).

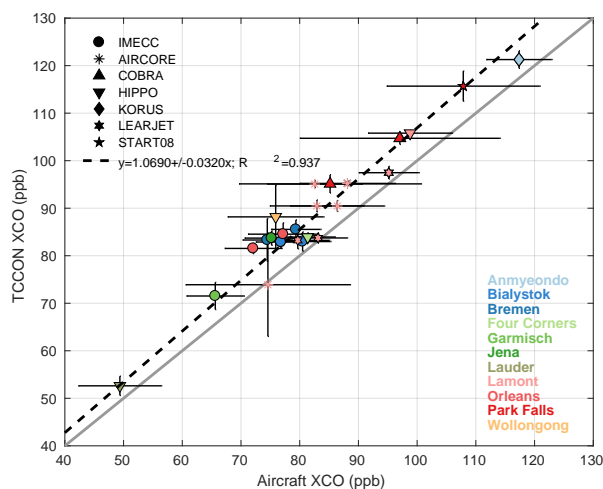


Figure S2. One-to-one plot comparing TCCON to aircraft measurements on the WMO. Before scaling to create the official TCCON product, column measurements are about 7 % higher than WMO scale. Courtesy of Matthäus Kiel.

S3 Small region approximation bin sizes

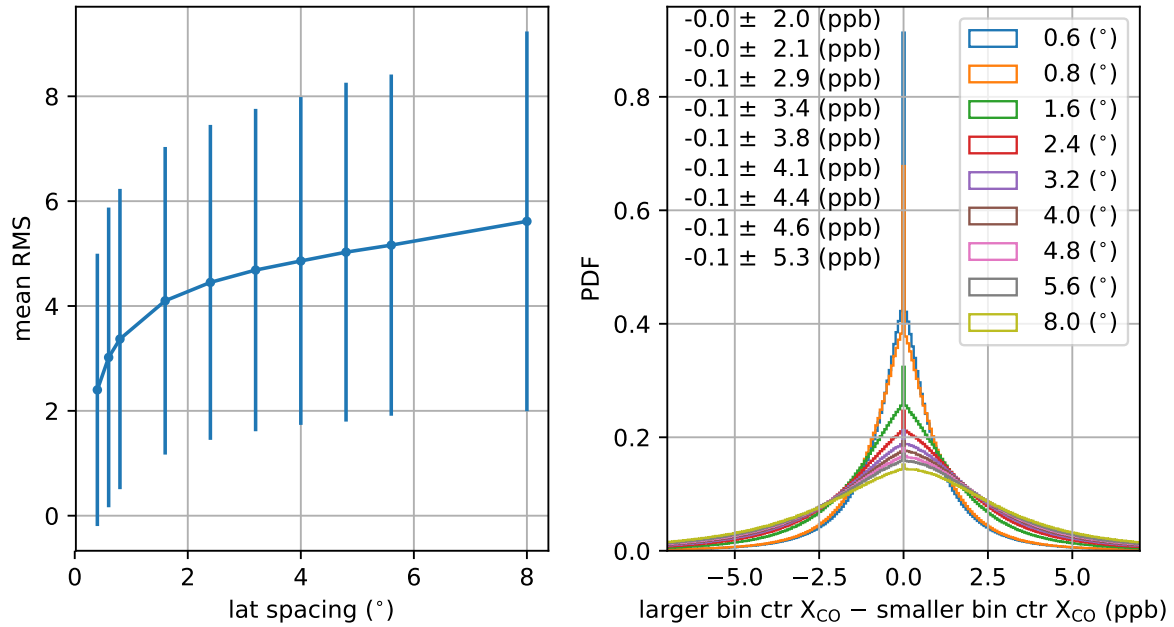


Figure S3. Results from using different SRA sizes. Left: The mean RMS as a function of bin size (latitude height). For larger bin sizes the mean RMS increases. Error bars are 1 . Right: Histograms of the difference in the center (median) X_{CO} values between larger bins and the smallest (0.4) bin. Text values are the mean deviations ± 1 . Smaller bins tend to have a median X_{CO} that is closer to the median X_{CO} of the (0.4) bin.

We examine the effects of the bin size on the small region approximation (SRA). Ten different bin sizes are compared all with a latitude:longitude ratio of 2:3 near the equator. Moving towards the poles, the latitude spacing is kept constant and the longitudinal width is increased to approximately maintain the same area size as at the equator. We examined areas with latitudinal spacings of 0.4, 0.6, 0.8, 1.6, 2.4, 3.2, 4.0, 4.8, 5.6, and 8.0 degrees. These were required to have a minimum of 6, 8, 10, 10, 10, 10, 10, 12, 15, and 25 points respectively for further analysis. We examine 1) the average root mean squared error compared with the center (median) X_{CO} point, and 2) the difference between the median X_{CO} for larger areas with the median X_{CO} for the 0.4 latitude areas with their center latitude and longitude inside the larger area (Fig. S3). For larger areas, the overall mean RMS increases. The spread of the difference between the median X_{CO} values between the larger and 0.4 bin increases with larger area bin size, but has little bias.

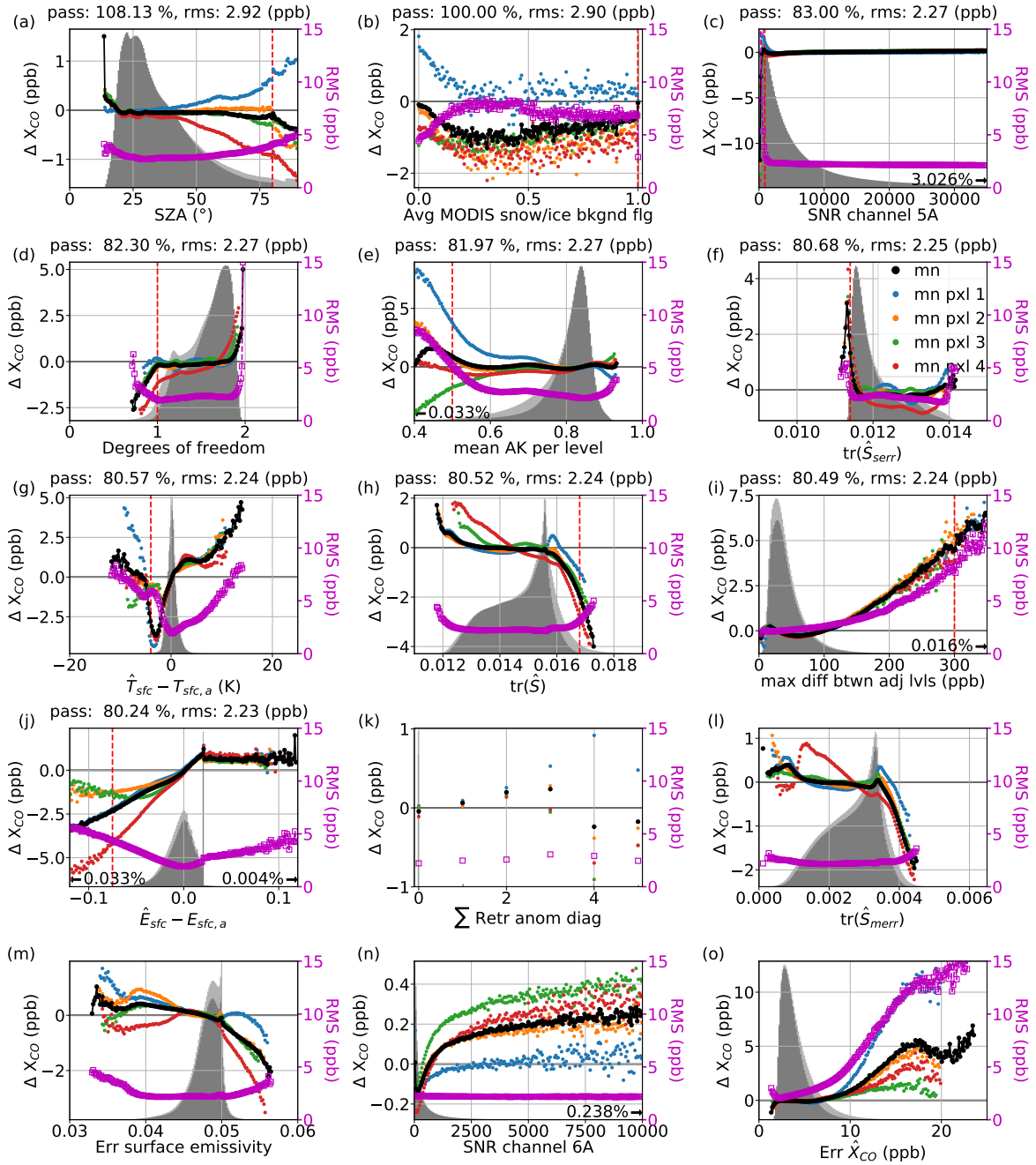


Figure S4. Diagrams showing the SRA bias as a function of one of the parameters in Table 3 in the main text for water. The black points show the overall mean bias (minimum 2000 points), the magenta points show the RMS, and the other points show the mean bias for the individual pixels (minimum 300 points). Red dashed lines indicate filter limits. (Continued on next page).

Figure S4. (Continued.) Lighter histograms for the first 2 plots (SZA and snow/ice flag) are of all the data, and for the remainder the lighter histograms are all data not excluded by the snow/ice and SZA filters. Darker histograms are of data not excluded by the SZA, the snow/ice, or any previous filters. Percentages with arrows at the bottom are for data outside the shown range. Data percentages at the top are compared with the snow/ice and SZA filtered data. QC filters applied to the first 10 plots. Plots are shown left to right and top to bottom in terms of more stringent or important filtering. Without any filtering and up to 9.6×10^8 (113.90% compared to SZA80 and no snow/ice), RMS=2.93 ppb.

S4 SRA relationships plots

We consider a variety of features for finding filter limits and checking for feature related bias based on the small region approximation (SRA). Figures S4 and S5 show fields that we opted to filter on, along with a few extra fields (such as SNR 6A) which we did not. Fields that were filtered on have text at the top. Various features of these plots are analyzed to determine if and where cutoffs should be made including the RMS, the overall mean bias, and the spread in bias among pixels. The underlying histograms give us a sense of how many observations will be removed at a certain cutoff. The mean SRA (black) also may be used to find systematic bias.

Figures S6, S7, S8, and S9 contains additional plots like those in Fig. S4–S5. The parameters along the x-axes in these plots were decided to be improper, or unhelpful to use as filter criteria.

The histograms in these figures allow us to check for the overall distribution of the data and find interesting features, of which we name a few. The difference in retrieved to surface emissivity over water ($E_{\text{sfc};a}$) is often 0.021 (Fig. S4j). This is because the a priori surface emissivity is 0.979 for all ocean scenes and the upper bound is 1.000 as higher values are unphysical (Merritt Deeter, personal communications August 22, 2018). We can see an average offset of about 0.007 from zero for this parameter over land (Fig. S5f). We see a similar offset of about 0.1K in $T_{\text{sfc};a}$ over land (Fig. S5m). Finally, the values of the histograms may be useful in themselves to get a sense of probability distributions. For example, distributions of degrees of freedom (Fig. S4d, S5k) and information bits (Fig. S6a, S8a) give a sense of the range of information content.

Figure S5. Similar to Fig. S4 but for land. QC filters applied to the first 11 plots. Without any filtering and up to $n = 2 \times 10^8$ (197.15% compared to SZA80 and no snow/ice), RMS=5.46 ppb.

Figure S6. Additional fields considered for fluxes over water part I. Diagrams showing the SRA bias as a function of one of various parameters either included in the MOPITT fields, derived from fields in the fields, or linked separately. Some of these parameters are listed in Table 3 in the main text. See also the caption to Fig. 3 and Fig. S4.

Figure S7. Additional fields considered for filters over water part II. These fields have some relation to MODIS. See also the caption to Figure S6.

Figure S8. Additional fields considered for filters over land part I. See also the caption to Figure S6.

Figure S9. Additional fields considered for filters over land part II. These fields have some relation to MODIS. See also the caption to Figure S7.

S5 Spatial locations of filtered data

We plot the spatial variability of where data are filtered based on our criteria in Sec. 3.3 in the main text. Generally it is desirable for data to be filtered uniformly globally unless there is a known geographical dependent feature that could cause significant uncertainty or bias, such as snow or ice. Figures S10 and S11 show the geographical locations of filters over water and land respectively. There is some geographical dependence, including low averaging kernels near the North pole, low degrees of freedom near the South Pole, and large deviations of surface temperature from the prior around western coastlines. Over land data from the Tibetan Plateau are screened by several filters. Filtering on the maximum difference between adjacent levels feature leads to a loss of some data over western China.

Figure S10. Maps of where data are filtered over water. Plots are of the percentage of data removed after all previous filters are applied. Order is first left to right, then top to bottom.

Figure S11. Maps of where data are filtered over land. Plots are of the percentage of data removed after all previous filters are applied. Order is first left to right, then top to bottom.

S6 Comparisons for each TCCON site

In Fig. S12 are the mean biases and standard deviation for each site using a variety of different methods to account for the different a priori profiles and averaging kernels. In general, there is not a clear and persistent difference from the various methods, possibly with the exception of the first and fourth columns (methods 0 and III), which on average appear larger.

- 5 Because the MOPITT to TCCON comparison can depend on the site, we include individual plots for sites here. In Fig. S13 the data are shown as annual plots with boxplots for each month. There is a wide variety of behavior depending on site. Many of the sites appear to have a seasonal cycle. However, we do not find a consistent pattern in these so we do not devise a bias correction based on a seasonally varying parameter.

S7 Bias compared with other data

- 10 We also check for any systematic trends in the MOPITT to TCCON difference with several co-observed fields of interest. A systematic trend could occur for example in the case of interfering species. Results are shown in Fig. S14. The interference of N_2O on the MOPITT retrieval has been discussed by Deeter et al. (2017). In the V7 algorithm a global linear trend with time is used for N_2O levels. When we subtract similar values $y = (0.06082x + 293.5)$, where x is months starting from January 1970) first the correlation increases slightly to $R^2 = 0.09$, and the magnitude of the slope increases to $0.17 \frac{X_{CO \text{ ppb}}}{X_{N_2O \text{ ppb}}}$. This is much larger than an estimate of $0.13 \frac{X_{CO \text{ ppb}}}{X_{N_2O \text{ ppb}}}$ based on the sensitivity test by Deeter et al. (2017) where the bias increased in the V6 retrieval by 3% which led to an decrease in the total column of about 1.2 ppb (based on Fig. 1 therein).
- 15

S8 Comparisons of retrieved to prior values

- The MOPITT prior is based on monthly averages from a Community Atmospheric Model with Chemistry (CAM-Chem) run from 2000–2009 (Buchholz et al., 2017). The model was gridded at 1° resolution. Assuming a linear change in emissions over model duration, 2004–2005 are the center years. If emissions have decreased from the 2004–2005 model years we would expect to see, to a first order, smaller retrieved than prior values. This is complicated by the averaging kernel matrix, as a change in the mixing ratio at one level can significantly affect the retrieved amount at other levels. For MOPITT profile retrievals, it is not uncommon to have larger off-diagonal elements than those on diagonal. A comparison of the retrieved to prior ratios (on a \log_2 scale) is shown in Fig. S15.
- 20

Figure S12. Average bias and standard deviation (black lines) for each site using the different methods described in Appendix D in the main text. Differences are converted to percent by dividing by the mean TCCON values. The bars on the far left are from a direct comparison of TCCON to MOPITT. The next four bars are from using a variety of different adjustments described as methods I–IV in Table D1 in the main text. The last eight bars are from treating a variety of different as “truth” and simulating the difference in errors. Sorted alphabetically.

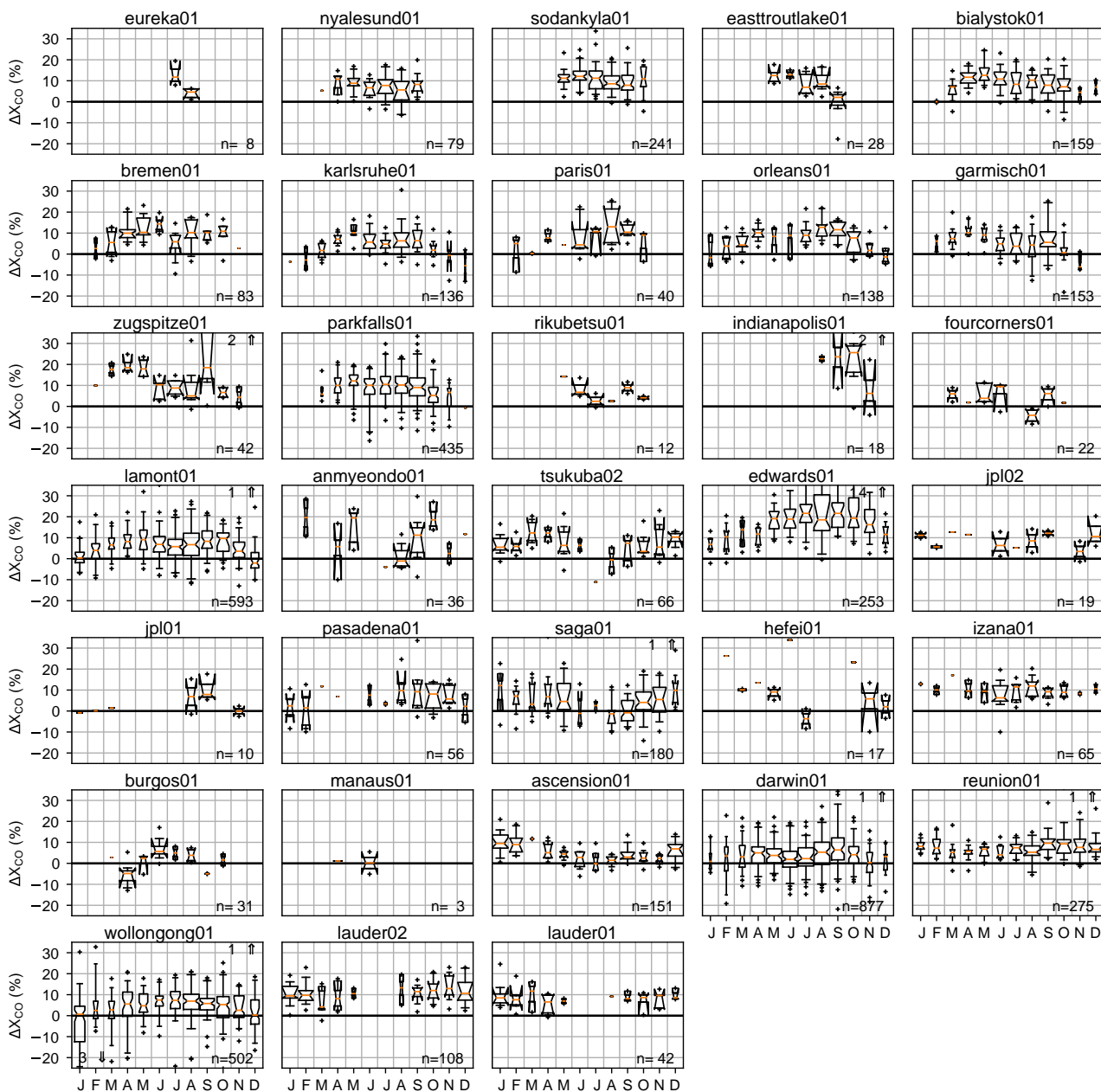


Figure S13. Seasonal variability in the difference between MOPITT and TCCON for all sites using method II. Data from all years are averaged for each month and shown as a box and whisker plot. Orange bars represent medians, and whiskers represent the central 95 % of data. Widths represent the relative amount of observations compared to other months for a given site. Notches represent the 95 % confidence interval on the median, as determined using the bootstrap method ($n = 5000$). Ordinate limits are fixed, so outliers are noted with numbers. Sorted by latitude.

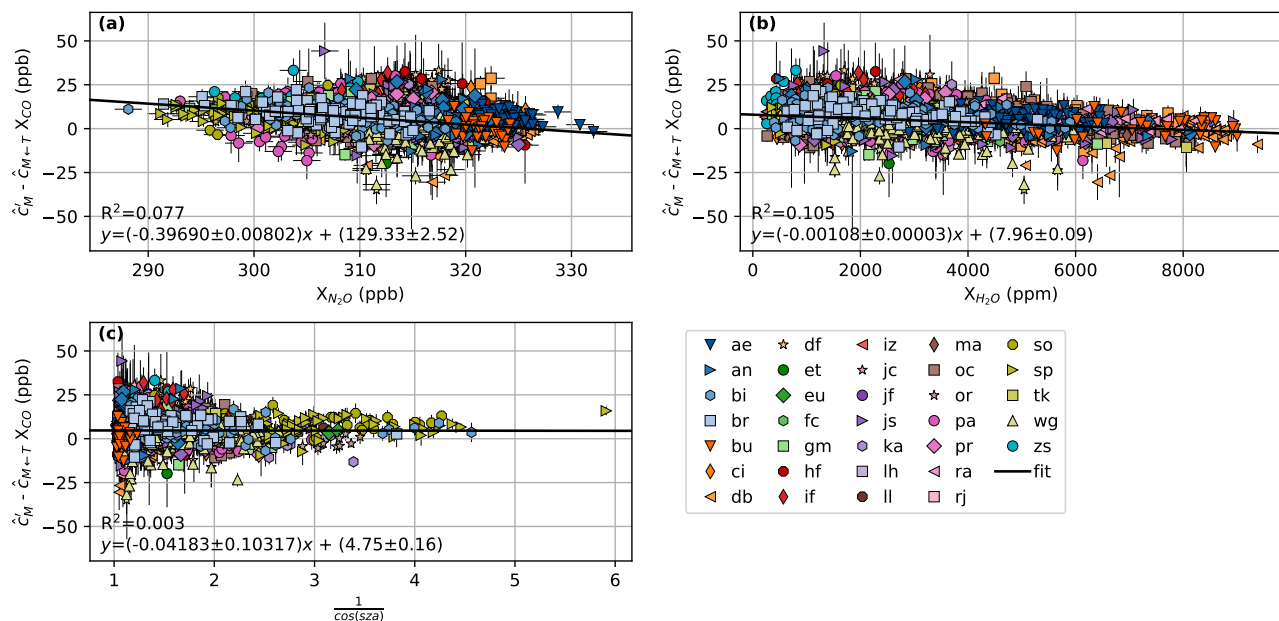


Figure S14. MOPITT TCCON differences using method II compared with fields of interest from the TCCON. R^2 values are for an ordinary least squares regression. Fits shown are from using the methods of York et al. (2004). **(a)** Versus X_{N_2O} retrieved from the TCCON. **(b)** Versus X_{H_2O} retrieved from the TCCON. **(c)** Difference data are plotted against an approximation of airmass.

References

- Buchholz, R. R., Deeter, M. N., Worden, H. M., Gille, J., Edwards, D. P., Hannigan, J. W., Jones, N. B., Paton-Walsh, C., Griffith, D. W. T., Smale, D., Robinson, J., Strong, K., Conway, S., Sussmann, R., Hase, F., Blumenstock, T., Mahieu, E., and Langerock, B.: Validation of MOPITT carbon monoxide using ground-based Fourier transform infrared spectrometer data from NDACC, *Atmospheric Measurement Techniques*, 10, 1927–1956, <https://doi.org/10.5194/amt-10-1927-2017>, 2017.
- Deeter, M. N., Edwards, D. P., Francis, G. L., Gille, J. C., Martínez-Alonso, S., Worden, H. M., and Sweeney, C.: A climate-scale satellite record for carbon monoxide: The MOPITT Version 7 product, *Atmospheric Measurement Techniques*, 10, 2533–2555, <https://doi.org/10.5194/amt-10-2533-2017>, 2017.
- GAW: GAW Report No. 192 Guidelines for the Measurement of Atmospheric Carbon Monoxide, Tech. Rep. 192, World Meteorological Organization, Global Atmospheric Watch, 2010.
- Novelli, P. C., Masarie, K. A., Lang, P. M., Hall, B. D., Myers, R. C., and Elkins, J. W.: Reanalysis of tropospheric CO trends: Effects of the 1997–1998 wildfires, *Journal of Geophysical Research*, 108, 4464, <https://doi.org/10.1029/2002JD003031>, 2003.
- York, D., Evensen, N. M., Martínez, M. L., and De Basabe Delgado, J.: Unified equations for the slope, intercept, and standard errors of the best straight line, *American Journal of Physics*, 72, 367–375, <https://doi.org/10.1119/1.1632486>, 2004.
- Zellweger, C., Buchmann, B., and Steinbrecher, R.: System and performance audit of surface ozone, carbon monoxide, methane and nitrous oxide at the global GAW station Jungfraujoch Switzerland, March 2015, Tech. rep., World Meteorological Organization, https://www.wmo.int/pages/prog/arep/gaw/documents/JFJ_2015.pdf%0A%0A, 2017.

